Renovating the electrode-electrolyte interphase for layered lithium- & manganese-rich oxides

Feng Wu [a,b,1], Weikang Li [a,1], Lai Chen [a,b,*], Yuefeng Su [a,b,**], Liying Bao [a], Wurigumula Bao [a], Zeliang Yang [a], Jing Wang [a], Yun Lu [a,b], Shi Chen [a]

[a] Beijing Key Laboratory of Environmental Science and Engineering, School of Materials Science and Engineering, Beijing Institute of Technology, Beijing, 100081, PR China
[b] Beijing Institute of Technology Chongqing Innovation Center, Chongqing, 401120, PR China

ABSTRACT

Layered lithium- & manganese-rich oxides (LMR), with their high capacity and cost-effective advantage, are considered as a potent alternative of the next-generation cathode material for lithium-ion batteries. The behaviors of the electrode-electrolyte interphase (EEI) are crucial to the electrochemical properties of LMR as a cathode material operating at wide voltage regions (from 2 to 4.8 V). Nonetheless, the understanding of EEI for LMR materials and the related renovation techniques are somewhat lacking. Herein, we gain insight into the EEI change mechanism for LMR materials during long electrochemical cycles and demonstrate a renovating method to mitigate its deterioration. As for the pristine electrode based on LMR materials, the increasing amount of $PO_xF_y^{z-}$ and metal fluorides lead to unpleasant degradation for both the EEI and the active material particle, causing evident performance decay. Whereas, the lithium phosphate, if employed in the electrode, effectively enhances the lithium ions transfer, impedes the decomposition of electrolyte salt, and leads to a more stable EEI, thus promoting the electrochemical performances of LMR materials. All results indicate that the EEI should be one of the critical components for comprehensively understanding the LMR material, and the success renovation by the lithium phosphate offers a new orientation for those intrinsic drawbacks of LMR material.

1. Introduction

Lithium-ion batteries (LIBs) are currently ones of the most widely used energy storage devices, especially for 3C products and electric vehicles [1–3]. However, the energy density of the LIBs is still insufficient for meeting the ever-growing demand from now to the future, and finding high-capacity alternatives as cathode materials for advanced LIBs becomes the critical issue to the present dilemma [4,5]. Layered lithium- & manganese-rich oxides (LMR), with significant advantages such as high mass energy density and low cost, attracted the attention from all over the world [6]. This kind of materials is usually written as $x\text{Li}_2\text{MnO}_3\cdot(1\text{-}x)\text{LiMO}_2$(M = Ni, Mn, and Co, so forth.) $(0.5 \leq x < 1.0)$, where lithium ions occupy both lithium layer and part of transition metal (TM) layer [7–9]. Although this unique structure provides high mass energy density, the concurrent issues such as voltage fade and inferior rate/cycle performances hamper the large-scale commercialization of LMR so far [10,11].

Most of the previous efforts such as structural design, coating, and doping were focused on the understanding and tuning the bulk structure evolutions of LMR [12–15]. While few reports focused on the electrode/electrolyte interphase (EEI), the concept of which is the inhomogeneous spatial region at the interface between two bulk phases in contact according to the Electrochemical Society (ECS). The property of EEI is critical to the overall electrochemical performance of LMR since a more extensive operating voltage range as 2.0–4.8V is usually applied [16,17]. Under this circumstance, the electrolyte solvent undergoes significant decompositions with evident side reactions [18]. Furthermore, previous research has confirmed that LMR suffers gas releasing during cycling, which is closely related to the anionic redox [19]. Highly active substances such as peroxide and superoxide put forward with higher

---

requirements to stabilize the EEI for LMR. Finally, the structural transformation of LMR material has been identified to extend from the surface to the bulk [20,21], which is also closely related to the interphase issue. Therefore, understanding the evolution process of EEI during electrochemical cycles is helpful to the ultimate utilization of LMR, and it is expected to solve their intractable electrochemical performances issues from the perspective of EEI [22,23].

Recently, phosphate-based salts have been applied to modify high energy cathode materials [24–26]. The coating of lithium phosphate [27–30] and Li-TM phosphate [31–33] brought practical improvements for LMR, but these modifications will come to naught since the pristine particles would lose contact with the coating layer because of the anisotropic volume change during the repeated lithiation and delithiation [34], making EEI dynamically changed and vulnerable [35]. Nonetheless, phosphate-based salts exhibit the potential to modify the property of interphases. Herein, we presented an in-depth theory of the relationship between the capacity decay/structure change of $Li_{1.2}Mn_{0.6}Ni_{0.2}O_2$ (LMNO), a typical LMR material, with the evolution of the EEI and further demonstrated that Nano-sized Li_3PO_4 (NLP) particles could renovate the EEI via a simple physical adding. Detailed analyses revealed that the NLP-containing EEI was more evenly distributed and thinner, which in turn prevented the continuous decomposition of $LiPF_6$ from the electrolyte, thereby alleviating the corrosion from the HF to the LMNO particles. This method differs from the previously reported coating or infusion methods with a more direct benefit, and further, we explain the furtherly effectiveness of phosphates on LMR material in a new way, which may direct the future path for layered cathode materials in solid-state batteries.

2. Material and methods

2.1. Synthesis & preparation

The LMR material with a chemical formula of $Li_{1.2}Mn_{0.6}Ni_{0.2}O_2$ was synthesized by a facile Sol-Gel method as reported before [36]. The nano-sized lithium phosphate (NLP) particles were synthesized via a sand grinding method: commercial lithium phosphate particles were mixed with the ethanol, then the mixture was ground for 5h in the sand grinder, then the mixed liquid was centrifuged, and the powder was dried in the oven at 80 °C to get the final NLP particles. More details of NLP are illustrated in Figure S1.

2.2. Materials characterization

X-ray diffraction was employed to check the crystal structure of synthesized samples, scanning between $2\theta = 10°–90°$ at a rate of $2°$/min (Rigaku, Model Ultima IV-185). The morphologies were checked by the field emission SEM (FEI QUANTA 250) and TEM (JEM-2100). The element distribution was checked on energy dispersive spectrometer attached on SEM. The X-ray photoelectron spectroscopy was conducted on PHI Quantera II. The solid-state nuclear magnetic resonance was performed on Agilent NMR Systems (600 MHz). The Raman and infrared spectra were checked by Renishaw inVia and Thermo Nicolet IS 10, respectively. The ToF-SIMs spectra were carried out by TESCAN instrument platform with ToF-SIMS analyzer. The acquisition was carried out at the ion beam energy of 20 Kev and 10 Kev with the current of 12 pA and 8 pA, the related covering the same field of view of 50×50 μm^2 and 8×8 μm^2 area. The mapping images consist of 192 pixels × 192 pixels. All the ex-situ tests were conducted with the electrodes after specific cycles, which was disassembled from the cells with several hours rest time to achieve the steady states (voltage change ≤ 0.001V/h).

2.3. Electrochemical test

The electrode was made by the doctor blade method, $Li_{1.2}Mn_{0.6}Ni_{0.2}O_2$ (LMNO) particles without/with NLP as the active material, and the acetylene black as conductive agent, were at first ground together for 20mins, then the PVDF dissolved in the NMP was added with another 10mins grinding before depositing the slurry on Al foil. The mass ratio of the active material, acetylene black and PVDF was controlled to 90:5:5, in which the active material included 99 wt% LMNO and 1 wt% NLP were named as 1%NLP, and so as the 2%NLP and other analogs. The wetting electrode was dried in a vacuum oven at 80 °C for 24h. The thickness of the as-prepared electrode was strictly managed to be ~50 μm by a rolling machine (MTI, MR-100A). The electrode loading density is ~5.0 mg cm^{-2} (see Supplementary Information Figure S2).

The electrolyte was 1 mol/L $LiPF_6$ dissolved in a mixture of ethylene carbonate and ethyl methyl carbonate (1:1 vol ratio), and the dosage was controlled by a pipette. The 2025 coin-type half-cells were assembled in a glove box filled with argon; the counter electrode was lithium metal, and the separator was the Celgard 2500. Galvanostatic tests were performed on CT2001A Land instruments (Wuhan, China) ranging from 2.0 V to 4.6 V at 30 °C in the thermostatic chamber. The current density of 250 mA g^{-1} was defined as 1C. Electrochemical impedance spectra (EIS) were tested on an SP-100 electrochemical workstation (Biologic, U.S.) at frequencies from 10^5 Hz to 0.01 Hz.

3. Results and discussion

The fundamental characteristics of the as-synthesized LMNO material are shown in Fig. 1. The General Structure Analysis System (GSAS) + EXPGUI suite was employed for the Rietveld refinement, as shown in Fig. 1(a) [37,38]. The crystal characteristics of both $R\overline{3}m$ and $C2/m$ were applied for the calculation. The observed and calculated values are highly consistent, where $\chi^2 = 1.86$. The XRD results (more data can be found in Table S1) illustrated that the LMNO materials own fine layered structure. Fig. 1(b) illustrates the Raman spectrum of the material, where two characteristic peaks of LMR between 500 and 600 cm^{-1} appeared. Also, the characteristic peak for the spinel structure is missing as the arrow points out in Fig. 1(b), which also indicates the pure layered structure of the as-synthesized LMNO [39]. Fig. 1(c) and (d) illustrate the results of SEM and TEM tests, respectively. It can be found that the material has a quasi-nanoscale morphology, and the particles are relatively uniform. The precise layer spacing of 0.475 nm in the high-resolution TEM image and the standard selected area electron diffraction (SAED) pattern in the inset imply the fine layered structure [40].

The effects of the NLP content on the electrochemical performances of $Li_{1.2}Mn_{0.6}Ni_{0.2}O_2$ were investigated carefully, and the optimized adding content of NLP was determined as 2%wt. as illustrated in Figure S3(a). Fig. 1(e) illustrates the specific capacity of the baseline and 2%NLP electrodes within 100 cycles with the corresponding coulombic efficiencies. The specific capacity of 2%NLP is higher than the baseline sample throughout the long cycling, and the capacity gap distinctly enlarges after 10 cycles. Another noteworthy point is that the coulombic efficiency fluctuation of 2%NLP is more stable than that of the baseline sample, which indicates the stability of the electrode as well. The rate performance of the two samples is shown in Fig. 1(f): 2%NLP owns better discharge capacity at higher rates than the baseline electrode. These differences between the baseline and 2%NLP electrodes lead to intensive investigations via several techniques in the following part (see more differences in Figure S3 and S4).

Previous researches proposed that the morphology of the electrode significantly affects its electrochemical performance [41]. The ideal electrode consists of the uniformly distributed active materials being interconnected by the integrated conductive network due to the conductive agents, and the binder can create a chain or mesh to preserve the former two [41,42]. The EEI can be analyzed preliminarily from the surface morphology of the electrode after certain cycles. Thus, SEM was employed, and the results are illustrated in Figure S5. Both electrodes show similar surface morphology before cycling. After 10 cycles, a thick cover was formed on the baseline electrode because of the reactions
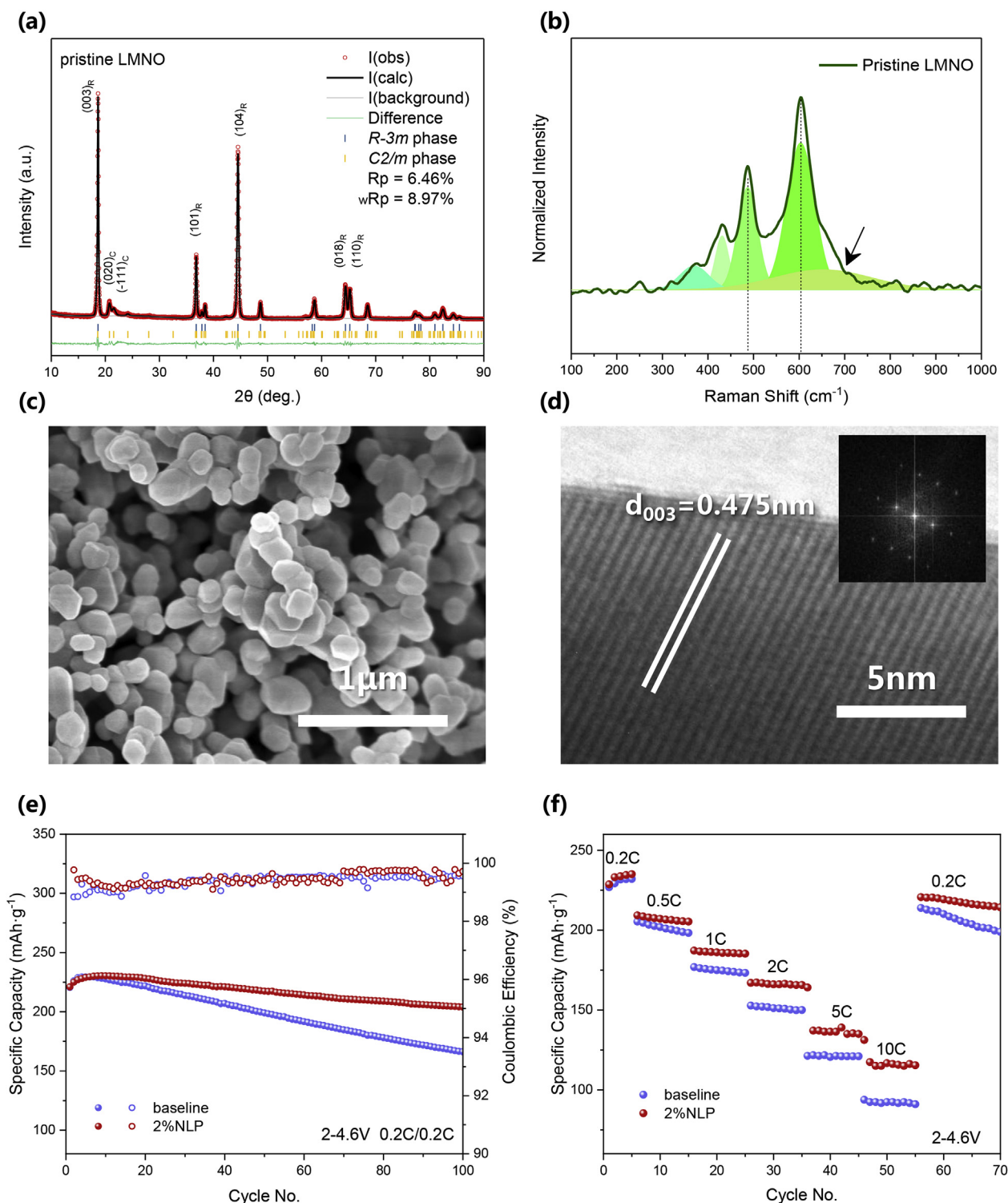
Fig. 1. Basic characterizations of the as-prepared $Li_{1.2}Mn_{0.6}Ni_{0.2}O_2$ (LMNO). (a) XRD figure of LMNO with the Rietveld refinement. (b) Raman spectrum of LMNO. (c) SEM figure of LMNO. (d) TEM figure with the SAED patterns of LMNO. Discharge specific capacity of the baseline and 2%NLP electrodes at (e) 0.2C and (f) different rates.

between the electrolyte and electrode, especially at the high voltage region [43]. The EEI on 2%NLP was thinner and more uniform than that of the baseline electrode. When progressed to the 20th cycle, both EEIs were attenuated, but that of 2%NLP kept smoother. After 100 cycles, the electrode of baseline sample appeared to have more cracks and more nonuniform by-products on the surface (the magnified images are shown in Figure S6), while that of the 2%NLP maintained as the original state.

The EDS mappings for the electrode surface corresponding to the selected cycles are shown as well. The distribution of elements in the baseline sample electrode changed: the mapping for phosphorus element enriched, while those for Mn and Ni diminished, and the fluorine and oxygen contents were presenting a downward trend as well. In contrast, for 2%NLP, the distribution of elements under different cycle did not show significant differences. Therefore, it can be inferred that different
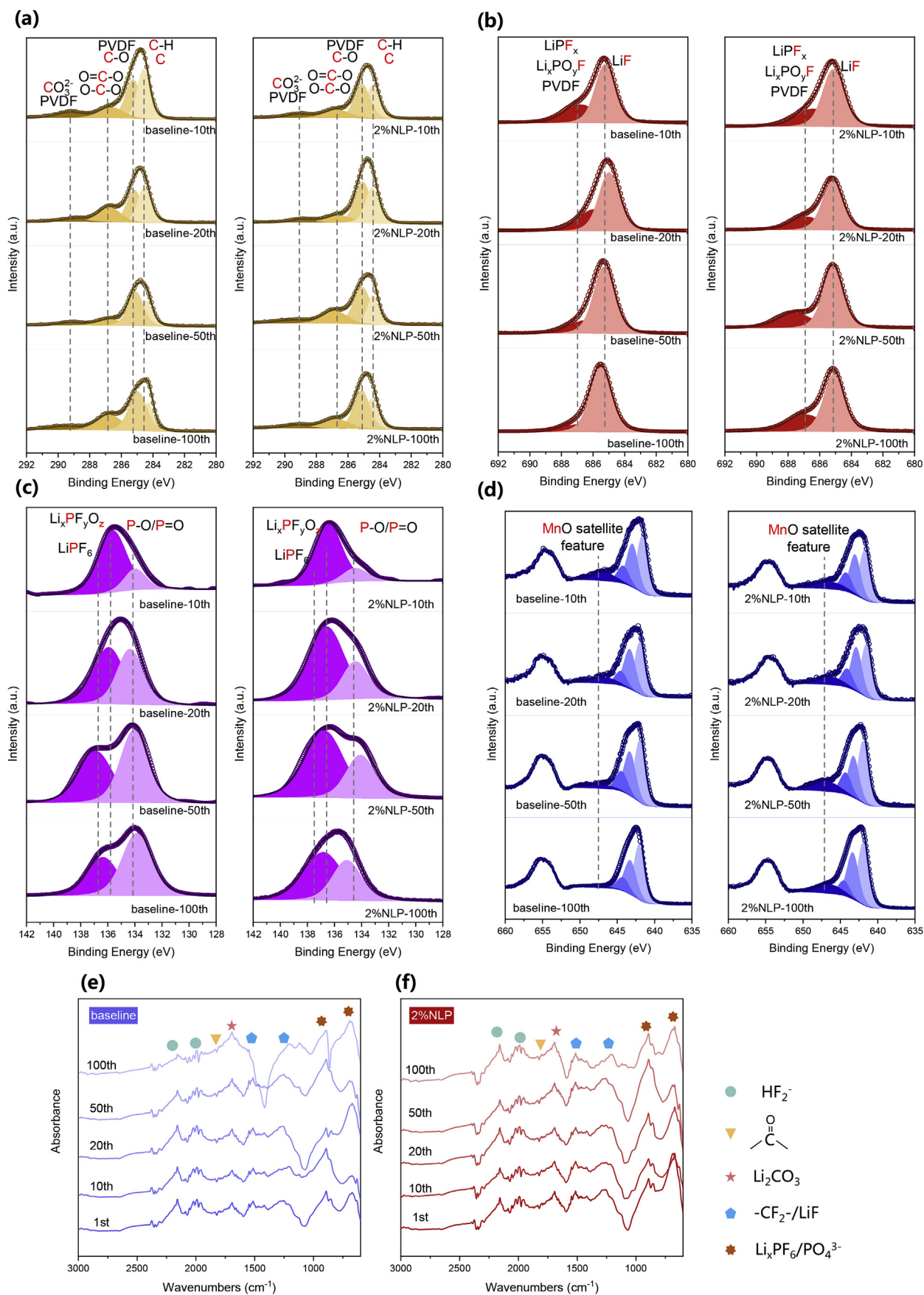
Fig. 2. XPS spectra of (a) C 1s, (b) F 1s, (c) P 2p and (d) Mn 2p, with the ATR-FTIR spectra of the (e) baseline and (f) 2%NLP electrodes after different cycles.
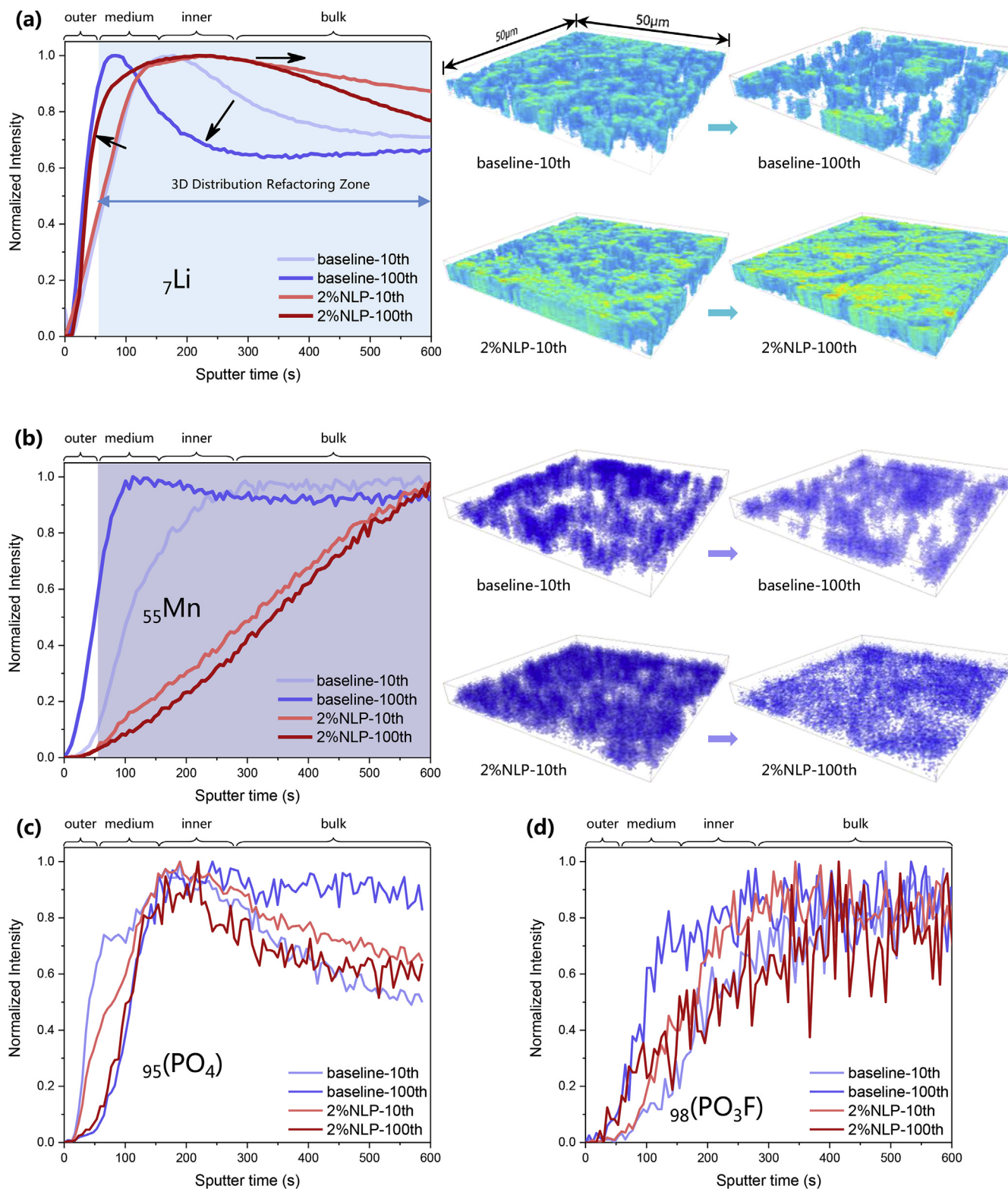
Fig. 3. ToF-SIMs depth profiles of (a) $_7$Li, (b) $_{55}$Mn (with the related 3D distribution refactoring models), (c) $_{95}$(PO$_4$) and (d) $_{98}$(PO$_3$F) from both the baseline and 2% NLP electrodes after 10th and 100th cycles. The full field of view is 50×50 μm^2.

changes occurred on the surfaces of the baseline and 2%NLP electrodes, which could be the significant reason for the gap of electrochemical performances.

X-ray photoelectron spectroscopy (XPS) and attenuated total reflection Fourier transform infrared spectroscopy (ATR-FTIR) were conducted to explore the details of the electrode surface, and the results are shown in Fig. 2. According to the XPS results in Fig. 2(a), carbonates in the form of lithium salts and other oligomers were generated at the surface of both electrodes, which may result in an increased impedance of the material [17,44]. The significant carbonyl signal (1687 cm^{-1}, marked by the yellow triangle) from ATR-FTIR in Fig. 2(e and f) appeared after the initial cycle, indicating the concentration of the electrolyte component
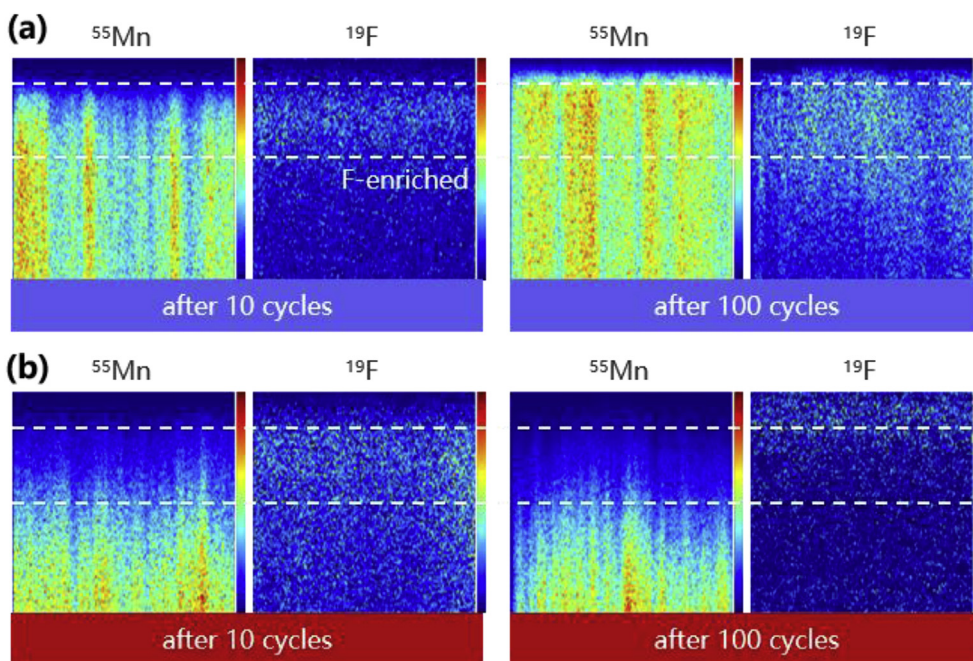
Fig. 4. Elemental distribution maps of $_7$Li, $_{55}$Mn from the (a) baseline and (b) 2%NLP electrodes from the front view with the full field view of 50×50 μm^2.

on the surface of the electrode [45–47]. Also, the red pentagram signal at ~1530 cm^{-1} represents the lithium carbonate [48], which may be introduced by the side reactions between LMNO and CO$_2$/H$_2$O during the preparation or the decomposition of the electrolyte during the charging/discharging. Combining the XPS results from C 1s, it can be speculated that the amount of lithium carbonate increases while the carbonyl amount decreases as the cycle progresses in the baseline electrode. As for 2%NLP, the NLP-containing EEI resisted this change, in which the carbonate kept in low content, and the carbonyl kept stable. As for the fluorine, a significant amount of metal fluoride was formed in the EEI since the enhanced intensity of F 1s at 685 eV in Fig. 2(b) for both kinds of the electrode [49]. The transition metal ions were only derived from the active material at the cathode side, and Li-ions from both cathode and anode sides. The F$^-$ ions would only come from the decomposition of PO$_x$F$_y^{z-}$ and the PVDF after attacked by oxygenated substances (such as trace H$_2$O) [44]. This standpoint can also be verified by the peak change of phosphorus in Fig. 2(c), that the peak represents P–O/P=O increased evidently for the baseline sample but not for 2%NLP. Combining the EDS mapping results in Figure S5, it can be concluded that PF$_6^-$ in the electrolyte was decomposed during cycles to form PO$_x$F$_y^{z-}$ (PF$_6^-$, PF$_5$, POF$_3$, PO$_2$F and so on) as components in the EEI, leading to the generation of F$^-$. The interphase in the baseline electrode contained vast fluorine element, which should be one of the major reasons for the electrochemical performance decay. As for 2%NLP, it was obvious that NLP help to restrain the decomposition of phosphorus-fluorine composite, due to the increasing of the signal representing P–O/P=O from P 2p spectra was suppressed, as well as the signal at 685 eV from F 1s spectra. Another important concern is the signal of –CF$_2$- that represents the binder (PVDF) in Fig. 2(e and f), which has large fluctuations in the late stage of cycling for the baseline sample while being stable in 2%NLP. The HF$_2^-$ signal is related to the surface stability of the interphase [50], and it can be seen that the HF$_2^-$ signal of the baseline sample was weakened with the cycles, but that of the 2%NLP sample kept stable in Fig. 2(e and f). This could be another proof that NLP assisted in forming stable interphase for LMNO particles.

Fig. 2(d) provided Mn 2p spectra from the baseline and 2%NLP at selected cycles. The splitting results of the 2p 3/2 peaks are provided to illustrate the details better. The peak at 646.8 eV can be remarked as the satellite feature of Mn^{2+} in Mn(II)O [51], although it's inaccurate to

quantify the content of Mn^{2+} in all manganese compound from this splitting results since the complexns of XPS signal of Mn 2p, changes from the relative intensity of this characteristic peak can be regarded as the existence of Mn^{2+} at the surface. The intensity of this satellite peak of the baseline electrode decreased as the cycles proceed, which can be explained by the dissolution of manganese oxides in the EEI caused by the corrosion of electrolyte. Meanwhile, the signal from 2%NLP kept well, confirming the robustness of the EEI with NLP. For a better understanding of all these resultants mentioned above, a typical Mosaic model [52] was illustrated in Figure S7(a). The diagram in Figure S7(b) is to better summarize the changes of each element and the related component during cycles. In short, NLP in the electrode suppressed the continuous formation of PO$_x$F$_y^{z-}$, and thus reducing the generation of undesirable by-products HF. More information including the fitting position and Full width at half maximum (FWHMs) using for the XPS fitting are listed in Table S2 (supplementary information).

The time-of-flight secondary ion mass spectrometry (ToF-SIMs) as the high-sensitive surface analysis technique was also applied on the surface of the electrode [34,53]. The total ToF-SIMs spectra of the baseline and 2%NLP electrodes after 10 cycles and 100 cycles are shown in Figure S8(a), with the verification of evenly distribution Ga$^+$ beam, and the typical SEM images of the electrode surface after the ToF-SIMs tests are shown in Figure S8(b and c). The results with different sizes of probe area are shown in Fig. 3, Fig. 4, and Figure S9. It is worth note that different matters responses differently when the ion beam focused. Thus the response signal for the ToF-SIMs could not correspond perfectly to the element depth distribution of every single etching area. Therefore, we defined the rapid escalating response signal comes from the outer layer of the interphase (sputter time was about 50s, and the corresponding curving depth was about 80 nm), as shown in Fig. 3, and the signal during ~50–150s and ~150–300s were regarded from the medium and inner layer of the interphase. After ~300s, the signal would come from the bulk particles with the interphases together. Here we applied 3D distribution refactoring to get a visualized lithium-ion distributions as Fig. 3(a) and (b) illustrated. The baseline sample had difference barely from 2%NLP after 10 cycles in the 50×50 μm^2 area, but the lithium content became too dispersive after 100 cycles, which means its uneven distribution. Moreover, the Mn distribution of 2%NLP owned an excellent correspondence with the Li distribution after 100 cycles, while the baseline
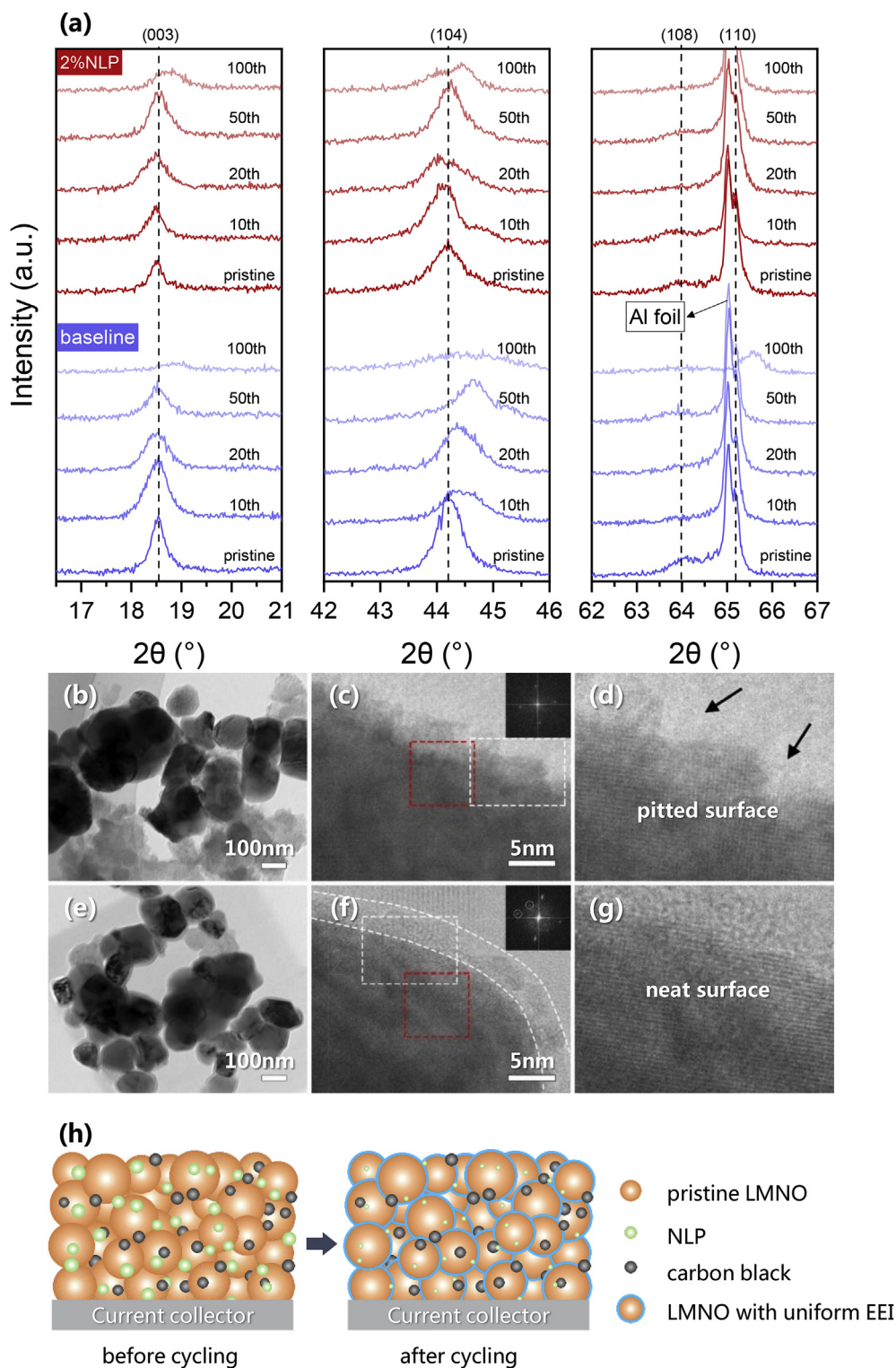
Fig. 5. (a) XRD patterns of the baseline and 2%NLP electrodes during different cycles at different 2θ = 16.5–21°, 42–46° and 62–67°, TEM images of cycled particles from the baseline (b–d) and 2%NLP (e–g) electrode, (h) the schematic of the electrode with NLP before and after cycling.

sample had not. Thus, it can be concluded that the Mn element dissolved from the active particle after long cycles and contributed to the formation of interphases. As for the $PO_xF_y^{z-}$ species, $_{95}(PO_4)$ and $_{98}(PO_3F)$ was detected, and the corresponding normalized intensity distributions are shown in Fig. 3(c) and (d). The distributions of $_{95}(PO_4)$ in both electrodes were very similar, only the baseline sample had a constant distributed content from the medium part to the bulk after 100 cycles, while other

samples had downward trends. However, the $_{98}(PO_3F)$ distribution of the baseline sample was enriched on the medium part after 100 cycles, while the 2% NLP sample remained unchanged, which verified the generation of these species on the interphases and matched the results of XPS and ATR-FTIR analyzes.

Meanwhile, Fig. 4 illustrates more details from the front views of Mn and F in both electrodes. The migration of Mn in the baseline sample was
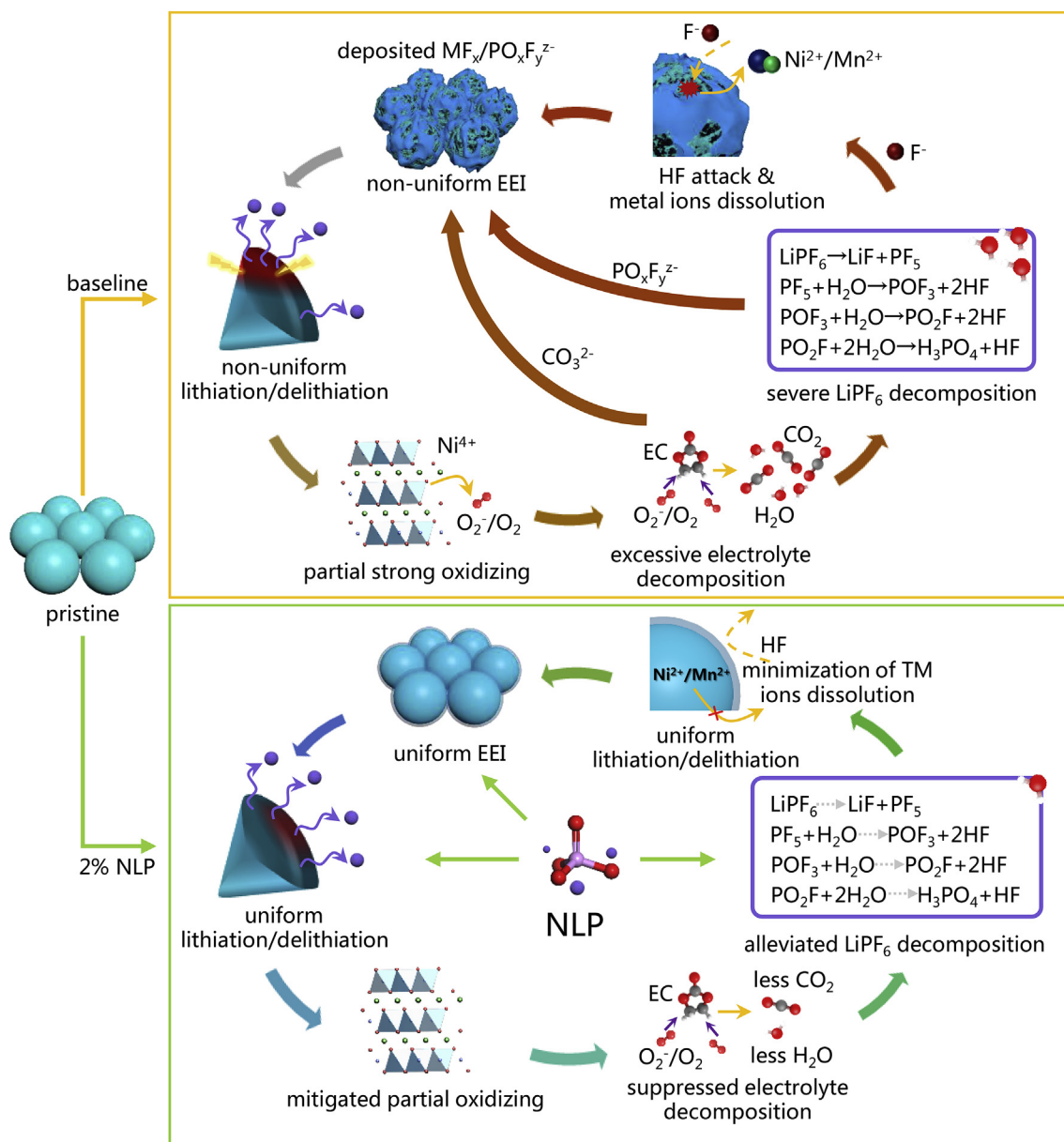
Fig. 6. Schematic of the electrode with and without NLP.

evident from the bulk to the medium surface in previous Fig. 3(b), which fitted the F element distribution from the front view, especially in the baseline electrode. The manganese element enriched at the outer and medium layer with the fluorine, and this trend became much more apparent after 100 cycles. On the contrary, 2%NLP withstood this change that no distinct enrichment of manganese and fluorine was detected from ToF-SIMs, as shown in Fig. 4(b). Thus, the dissolution of Mn ions is directly correlated to the fluorine, and the stability of the interphase is of great importance.

As mentioned before, the unwilling dissolution of transition metal ions from LMNO particles leads to the attenuation of electrochemical performances, which would be proofed by the XRD results as well. Herein, we exhibited how EEI effect the crystal characteristics of LMNO after selected cycles on the baseline sample and 2%NLP in Fig. 5 with the full view in Figure S10. The (003) and (104) peaks of the baseline electrode shifted to higher angles and became very weak after 100 cycles in Fig. 5(a), indicating the degradation of layered features, which can be inferred to the partial structure changes from layered to spinel and rock-salt type. In contrast, the 2%NLP electrode still possessed a distinct peak

intensity, representing the well-retained layered features. Furthermore, the splitting of (108)/(110) peaks is also a manifestation of layered features, where 2%NLP retained better after cycling. It can be speculated from the XRD patterns that NLP helps to inhibit the phase transition process of LMNO. HRTEM results of the cycled materials (100 cycles @ 1C) on both electrodes are illustrated as well, where Fig. 5(b–d) is for the baseline sample, and Fig. 5(e–g) is for 2%NLP sample. Fig. 5(b) and (e) exhibit the overall view of particles after cycling, where the surface of the particles in the baseline sample lacking covering, with the evident agglomeration of amorphous substance. The surface of the 2% NLP particles possessed a very uniform EEI with a thickness of ~3 nm, which contributed the protective effect on the active material (magnified view in Fig. 5(c) and (f). The area in the red dotted frame was selected to carry out fast Fourier transform (FFT), and the results are illustrated in the inset, indicating that crystal characteristics of 2%NLP were better preserved. Fig. 5(d) and (g) are the enlarged patterns of the white dotted frame, the surface of the baseline material was severely pitted, it can be confirmed that metal elements such as Mn and Ni were dissolved in the electrolyte since severe F⁻ attack when combining the ToF-SIMs results,

this dissolution directly led to capacity decay [54]. On the contrary, the surface of the 2%NLP material is relatively smooth, indicating that NLP can well alleviate the erosion from the electrolyte for the active material through inducing stable interphase on the surface, as Fig. 5(h) illustrated.

Electrochemical impedance spectroscopy (EIS) and cyclic voltammetry (CV) measurements were conducted to gain further insight into the effects of NLP on the electrochemical behavior of LMNO. Figure S11(a) and (b) show the Nyquist plots of the baseline sample and 2%NLP, respectively. All the spectra exhibit two semicircles corresponding to the charge transfer resistance (R_{ct}) and mass transfer process (R_f) [55]. The formation of EEI was slow at the beginning, which is positively correlated with the charge transfer impedance, i.e., the thicker and denser EEI, the larger R_{ct}. Also, the R_f value is naturally increasing with the cycles; the growth rate of R_f from 2%NLP is slower, which also indicates that NLP is beneficial to the stability of the electrode. The CV results are shown in Figure S11(c) and (d), recorded at 0.1 mV s^{-1} in the voltage range of 2–4.6V for initial three cycles. Two visible oxidation peaks appear at 3.87V and 4.14V, which can be ascribed to the oxidation of Ni^{2+}/Ni^{4+}; another peak appears at 4.5V, corresponding to the electrochemical activation of Li$_2$MnO$_3$ phase [56]. It is worth noting that 2%NLP possesses better overlapping reduction peaks, suggesting the better stability of the electrode. As a result, the cycle and rate performances of 2%NLP were enhanced.

According to the above spectral and structural analyses, we summarized the evolution process of the LMNO's EEI and the mechanism of its tailoring by NLP, as shown in Fig. 6. It is known that the material itself with the electrode fabrication process will influence the intercalating/deintercalating uniformity of lithium-ions. While during high-voltage cycling, not only the electrolyte is more readily decomposed, but also the highly oxidized ions such as O$_x^{y-}$, which derived from local immoderate delithiation at the surface of LMR, will further accelerate the decomposition of the electrolyte, and produce more carbon dioxide and trace water, thereby accelerating the decomposition of LiPF$_6$. When a large amount of free HF and PO$_x$F$_y^{z-}$ substances are generated, the free F ions will erode the surface of the cathode material, especially where EEI is not protected as covers for active particles, resulting in the dissolution of the transition metal ions. This undesired dissolution leads to porous defects on the surface, which may adsorb more F$^-$ ions to accelerate the corrosion [54,57]. The resulted metal fluorides will then attach to the electrode surface such that the interphase impedance increases, which in turn causes degradation of the EEI. This vicious cycle, as shown in Fig. 6, can cause rapid degradation of the performance of the LMR electrode. Therefore, it is more significant for LMR materials to own stable EEI since it is a self-promoting degradation process. The attacks from the decomposed electrolyte to the cathode material will become more aggravated once the decomposition of electrolyte begins. Fortunately, we found that when a little bit of NLP was added to the electrode, the stability of the EEI can be improved, thus contributing to the stability of LMR and the entire electrode. More importantly, the stabilized EEI suppresses the bulk phase transformations, which suggests a new insight to understand the decay mechanism of LMR material.

4. Conclusion

The EEI of electrodes based on LMR material has been investigated through the long electrochemical cycles with its renovating by lithium phosphate particles. The results indicate that the EEI of the pristine electrode is highly unstable, and the excessive generation of metal fluoride/PO$_x$F$_y^{z-}$ leads to a vicious circle of electrochemical degradation. To alleviate these shortcomings, we utilized lithium phosphate directly to the electrode. It was found that lithium phosphate, on the one hand, facilitated to the uniform transfer of lithium ions because of its natural solid-state electrolyte property; on the other hand, suppressed the continuous generation of PO$_x$F$_y^{z-}$, in which the by-products are the undesirable HF. Therefore, the electrode-electrolyte interphase which would be generated during the cycling was successfully renovated, and

the electrochemical performances of Li$_{1.2}$Mn$_{0.6}$Ni$_{0.2}$O$_2$ have been improved. In brief, we believe that an in-depth understanding of the EEI with the valid renovation are both essential for designing high specific energy cathode based on LMR materials.

Declaration of competing interest

There are no conflicts to declare.

Appendix A. Supplementary data

Supplementary data to this article can be found online at https://doi.org/10.1016/j.ensm.2019.12.017.

References

[1] M. Armand, J.M. Tarascon, Building better batteries, Nature (2008), https://doi.org/10.1038/451652a.
[2] J. Lu, Z. Chen, Z. Ma, F. Pan, L.A. Curtiss, K. Amine, The role of nanotechnology in the development of battery materials for electric vehicles, Nat. Nanotechnol. (2016), https://doi.org/10.1038/nnano.2016.207.
[3] S. Muhammad, H. Kim, Y. Kim, D. Kim, J.H. Song, J. Yoon, J.H. Park, S.J. Ahn, S.H. Kang, M.M. Thackeray, W.S. Yoon, Evidence of reversible oxygen participation in anomalously high capacity Li- and Mn-rich cathodes for Li-ion batteries, Nano Energy (2016), https://doi.org/10.1016/j.nanoen.2015.12.027.
[4] K. Turcheniuk, D. Bondarev, V. Singhal, G. Yushin, Ten years left to redesign lithium-ion batteries, Nature (2018), https://doi.org/10.1038/d41586-018-05752-3.
[5] W. Li, B. Song, A. Manthiram, High-voltage positive electrode materials for lithium-ion batteries, Chem. Soc. Rev. (2017), https://doi.org/10.1039/c6cs00875e.
[6] F. Wu, N. Li, Y. Su, H. Shou, L. Bao, W. Yang, L. Zhang, R. An, S. Chen, Spinel/layered heterostructured cathode material for high-capacity and high-rate Li-ion batteries, Adv. Mater. (2013), https://doi.org/10.1002/adma.201300598.
[7] H.D. Liu, Y. Chen, S. Hy, K. An, S. Venkatachalam, D.N. Qian, M.H. Zhang, Y.S. Meng, Operando lithium dynamics in the Li-rich layered oxide cathode material via neutron diffraction, Advanced Energy Materials (2016), https://doi.org/10.1002/aenm.201502143.
[8] L. Chen, S. Chen, D.Z. Hu, Y.F. Su, W.K. Li, Z. Wang, L.Y. Bao, F. Wu, Crystal structure and electrochemical performance of lithium-rich cathode materials xLi2MnO3· (1-x)LiNi0.5Mn0.5O2 (x=0.1-0.8), Wuli Huaxue Xuebao/Acta Physico - Chimica Sinica (2014), https://doi.org/10.3866/PKU.WHXB201312252.
[9] S. Hy, H.D. Liu, M.H. Zhang, D.N. Qian, B.J. Hwang, Y.S. Meng, Performance and design considerations for lithium excess layered oxide positive electrode materials for lithium ion batteries, Energy Environ. Sci. (2016), https://doi.org/10.1039/c5ee03573b.
[10] M.D. Radin, S. Hy, M. Sina, C.C. Fang, H.D. Liu, J. Vinckeviciute, M.H. Zhang, M.S. Whittingham, Y.S. Meng, A. Van der Ven, Narrowing the gap between theoretical and practical capacities in Li-ion layered oxide cathode materials, Advanced Energy Materials (2017), https://doi.org/10.1002/aenm.201602888.
[11] F.A. Susai, H. Sclar, Y. Shilina, T.R. Penki, R. Raman, S. Maddukuri, S. Maiti, I.C. Halalay, S. Luski, B. Markovsky, D. Aurbach, Horizons for Li-ion batteries relevant to electro-mobility: high-specific-energy cathodes and chemically active separators, Adv. Mater. (2018), https://doi.org/10.1002/adma.201801348.
[12] L. Chen, Y. Su, S. Chen, N. Li, L. Bao, W. Li, Z. Wang, M. Wang, F. Wu, Hierarchical Li$_{1.2}$Ni0.2Mn0.6O2 nanoplates with exposed {010} planes as high-performance cathode material for lithium-ion batteries, Adv. Mater. (2014), https://doi.org/10.1002/adma.201402541.
[13] B. Wu, X.K. Yang, X. Jiang, Y. Zhang, H.B. Shu, P. Gao, L. Liu, X.Y. Wang, Synchronous tailoring surface structure and chemical composition of Li-Rich-Layered oxide for high-energy lithium-ion batteries, Adv. Funct. Mater. (2018), https://doi.org/10.1002/adfm.201803392.
[14] X. Zheng, X. Wang, X. Cai, L. Xing, M. Xu, M. Liao, X. Li, W. Li, Constructing a protective interface film on layered lithium-rich cathode using an electrolyte additive with special molecule structure, ACS Appl. Mater. Interfaces (2016), https://doi.org/10.1021/acsami.6b09554.
[15] J.G. Han, S.J. Lee, J. Lee, J.S. Kim, K.T. Lee, N.S. Choi, Tunable and robust phosphite-derived surface film to protect lithium-rich cathodes in lithium-ion batteries, ACS Appl. Mater. Interfaces (2015), https://doi.org/10.1021/acsami.5b01770.
[16] K.J. Carroll, D. Qian, C. Fell, S. Calvin, G.M. Veith, M. Chi, L. Baggetto, Y.S. Meng, Probing the electrode/electrolyte interface in the lithium excess layered oxide

$Li_{1.2}Ni_{0.2}Mn_{0.6}O_2$, Phys. Chem. Chem. Phys. (2013), https://doi.org/10.1039/c3cp51927a.

[17] M. Gauthier, T.J. Carney, A. Grimaud, L. Giordano, N. Pour, H.H. Chang, D.P. Fenning, S.F. Lux, O. Paschos, C. Bauer, F. Maglia, S. Lupart, P. Lamp, Y. Shao-Horn, Electrode-electrolyte interface in Li-ion batteries: current understanding and new insights, J. Phys. Chem. Lett. (2015), https://doi.org/10.1021/acs.jpclett.5b01727.

[18] C.C. Ye, W.Q. Tu, L.M. Yin, Q.F. Zheng, C. Wang, Y.T. Zhong, Y.G. Zhang, Q.M. Huang, K. Xu, W.S. Li, Converting detrimental HF in electrolytes into a highly fluorinated interphase on cathodes, J. Mater. Chem. (2018), https://doi.org/10.1039/c8ta06150e.

[19] K. Luo, M.R. Roberts, R. Hao, N. Guerrini, D.M. Pickup, Y.S. Liu, K. Edstrom, J. Guo, A.V. Chadwick, L.C. Duda, P.G. Bruce, Charge-compensation in 3d-transition-metal-oxide intercalation cathodes through the generation of localized electron holes on oxygen, Nat. Chem. (2016), https://doi.org/10.1038/nchem.2471.

[20] D. Mohanty, J.L. Li, D.P. Abraham, A. Huq, E.A. Payzant, D.L. Wood, C. Daniel, Unraveling the voltage-fade mechanism in high-energy-density lithium-ion batteries: origin of the tetrahedral cations for spinel conversion, Chem. Mater. (2014), https://doi.org/10.1021/cm5031415.

[21] A. Boulineau, L. Simonin, J.F. Colin, C. Bourbon, S. Patoux, First evidence of manganese-nickel segregation and densification upon cycling in Li-rich layered oxides for lithium batteries, Nano Lett. (2013), https://doi.org/10.1021/nl4019275.

[22] K. Xu, Electrolytes and interphases in Li-ion batteries and beyond, Chem. Rev. (2014), https://doi.org/10.1021/cr500003w.

[23] Z.W. Yin, X.X. Peng, J.T. Li, C.H. Shen, Y.P. Deng, Z.G. Wu, T. Zhang, Q.B. Zhang, Y.X. Mo, K. Wang, L. Huang, H. Zheng, S.G. Sun, Revealing of the activation pathway and cathode electrolyte interphase evolution of Li-rich $0.5Li_2MnO_3·0.5LiNi_{0.3}Co_{0.3}Mn_{0.4}O_2$ cathode by in situ electrochemical quartz crystal microbalance, ACS Appl. Mater. Interfaces (2019), https://doi.org/10.1021/acsami.9b02236.

[24] Y. Zhao, J.T. Liu, S.B. Wang, R. Ji, Q.B. Xia, Z.P. Ding, W.F. Wei, Y. Liu, P. Wang, D.G. Ivey, Surface structural transition induced by gradient polyanion-doping in Li-rich layered oxides: implications for enhanced electrochemical performance, Adv. Funct. Mater. (2016), https://doi.org/10.1002/adfm.201600576.

[25] P.F. Yang, J.M. Zheng, S. Kuppan, Q.Y. Li, D.P. Lv, J. Xiao, G.Y. Chen, J.G. Zhang, C.M. Wang, Phosphorus enrichment as a new composition in the solid electrolyte interphase of high-voltage cathodes and its effects on battery cycling, Chem. Mater. (2015), https://doi.org/10.1021/acs.chemmater.5b03510.

[26] B. Xiao, B. Wang, J. Liu, K. Kaliyappan, Q. Sun, Y. Liu, G. Dadheech, M.P. Balogh, L. Yang, T.-K. Sham, R. Li, M. Cai, X. Sun, Highly stable $Li_{1.2}Mn_{0.54}Co_{0.13}Ni_{0.13}O_2$ enabled by novel atomic layer deposited $AlPO_4$ coating, Nano Energy (2017), https://doi.org/10.1016/j.nanoen.2017.02.015.

[27] I.T. Kim, J.C. Knight, H. Celio, A. Manthiram, Enhanced electrochemical performances of Li-rich layered oxides by surface modification with reduced graphene oxide/$AlPO_4$ hybrid coating, J. Mater. Chem. (2014), https://doi.org/10.1039/c4ta00898g.

[28] Y. Lee, K.E. Lee, K.Y. Lee, J. Mun, J.K. Lee, W. Choi, Facile formation of a Li_3PO_4 coating layer during the synthesis of a lithium-rich layered oxide for high-capacity lithium-ion batteries, J. Power Sources (2016), https://doi.org/10.1016/j.jpowsour.2016.03.024.

[29] H. Liu, C. Chen, C.Y. Du, X.S. He, G.P. Yin, B. Song, P.J. Zuo, X.Q. Cheng, Y.L. Ma, Y.Z. Gao, Lithium-rich $Li_{1.2}Ni_{0.13}Co_{0.13}Mn_{0.54}O_2$ oxide coated by Li_3PO_4 and carbon nanocomposite layers as high performance cathode materials for lithium ion batteries, J. Mater. Chem. (2015), https://doi.org/10.1039/c4ta04823g.

[30] H. Liu, J. Huang, D. Qian, S. Hy, C. Fang, J. Luo, Y.S. Meng, Communication—enhancing the electrochemical performance of lithium-excess layered oxide $Li_{1.13}Ni_{0.3}Mn_{0.57}O_2$ via a facile nanoscale surface modification, J. Electrochem. Soc. (2016), https://doi.org/10.1149/2.0821606jes.

[31] Q.Q. Qiao, H.Z. Zhang, G.R. Li, S.H. Ye, C.W. Wang, X.P. Gao, Surface modification of Li-rich layered $Li(Li_{0.17}Ni_{0.25}Mn_{0.58})O_2$ oxide with Li–Mn–PO_4 as the cathode for lithium-ion batteries, J. Mater. Chem. (2013), https://doi.org/10.1039/c3ta00028a.

[32] D. Shin, C. Wolverton, J.R. Croy, M. Balasubramanian, S.H. Kang, C.M.L. Rivera, M.M. Thackeray, First-principles calculations, electrochemical and X-ray absorption studies of Li-Ni-PO_4 surface-treated $xLi_2MnO_3·(1−x)LiMO_2$ (M = Mn, Ni, Co) electrodes for Li-ion batteries, J. Electrochem. Soc. (2011), https://doi.org/10.1149/2.098202jes.

[33] M.-J. Lee, E. Lho, P. Oh, Y. Son, J. Cho, Simultaneous surface modification method for $0.4Li_2MnO_3·0.6LiNi_{1/3}Co_{1/3}Mn_{1/3}O_2$ cathode material for lithium ion batteries: acid treatment and $LiCoPO_4$ coating, Nano Research (2017), https://doi.org/10.1007/s12274-017-1662-8.

[34] J. Li, W. Li, Y. You, A. Manthiram, Extending the service life of high-Ni layered oxides by tuning the electrode-electrolyte interphase, Advanced Energy Materials (2018), https://doi.org/10.1002/aenm.201801957.

[35] L.P. Wang, X.D. Zhang, T.S. Wang, Y.X. Yin, J.L. Shi, C.R. Wang, Y.G. Guo, Ameliorating the interfacial problems of cathode and solid-state electrolytes by interface modification of functional polymers, Advanced Energy Materials (2018), https://doi.org/10.1002/aenm.201801528.

[36] F. Wu, W.K. Li, L. Chen, Y. Lu, Y.F. Su, W. Bao, J. Wang, S. Chen, L.Y. Bao, Polyacrylonitrile-polyvinylidene fluoride as high-performance composite binder for layered Li-rich oxides, J. Power Sources (2017), https://doi.org/10.1016/j.jpowsour.2017.05.063.

[37] A.C. Larson, R.B. Von Dreele, GSAS. General Structure Analysis System, 1994.

[38] B.H. Toby, EXPGUI, a graphical user interface for GSAS, J. Appl. Crystallogr. (2001), https://doi.org/10.1107/S0021889801002242.

[39] M. Xu, L.F. Fei, W. Lu, Z.Y. Chen, T. Li, Y. Liu, G.Y. Gao, Y.Q. Lai, Z.A. Zhang, P. Wang, H.T. Huang, Engineering hetero-epitaxial nanostructures with aligned Li-ion channels in Li-rich layered oxides for high-performance cathode application, Nano Energy (2017), https://doi.org/10.1016/j.nanoen.2017.03.051.

[40] J.M. Zheng, P.H. Xu, M. Gu, J. Xiao, N.D. Browning, P.F. Yan, C.M. Wang, J.G. Zhang, Structural and chemical evolution of Li- and Mn-rich layered cathode material, Chem. Mater. (2015), https://doi.org/10.1021/cm5045978.

[41] B.W. Xiao, X.L. Sun, Surface and subsurface reactions of lithium transition metal oxide cathode materials: an overview of the fundamental origins and remedying approaches, Advanced Energy Materials (2018), https://doi.org/10.1002/aenm.201802057.

[42] N.J. Dudney, J. Li, Materials science. Using all energy in a battery, Science (2015), https://doi.org/10.1126/science.aaa2870.

[43] R. Tatara, P. Karayaylali, Y. Yu, Y. Zhang, L. Giordano, F. Maglia, R. Jung, J.P. Schmidt, I. Lund, Y. Shao-Horn, The effect of electrode-electrolyte interface on the electrochemical impedance spectra for positive electrode in Li-ion battery, J. Electrochem. Soc. (2018), https://doi.org/10.1149/2.0121903jes.

[44] J.G. Han, K. Kim, Y. Lee, N.S. Choi, Scavenging materials to stabilize $LiPF_6$-containing carbonate-based electrolytes for Li-ion batteries, Adv. Mater. (2018), https://doi.org/10.1002/adma.201804822.

[45] D. Aurbach, M.D. Levi, E. Levi, H. Teller, B. Markovsky, G. Salitra, U. Heider, L. Heider, Common electroanalytical behavior of Li intercalation processes into graphite and transition metal oxides, J. Electrochem. Soc. (1998), https://doi.org/10.1149/1.1838758.

[46] M.Q. Xu, L.S. Hao, Y.L. Liu, W.S. Li, L.D. Xing, B. Li, Experimental and theoretical investigations of dimethylacetamide (DMAc) as electrolyte stabilizing additive for lithium ion batteries, J. Phys. Chem. C (2011), https://doi.org/10.1021/jp109562u.

[47] Y. Dong, B.T. Young, Y. Zhang, T. Yoon, D.R. Heskett, Y. Hu, B.L. Lucht, Effect of lithium borate additives on cathode film formation in $LiNi_{0.5}Mn_{1.5}O_4$/Li cells, ACS Appl. Mater. Interfaces (2017), https://doi.org/10.1021/acsami.7b01481.

[48] M.Q. Xu, L. Zhou, L.S. Hao, L.D. Xing, W.S. Li, B.L. Lucht, Investigation and application of lithium difluoro(oxalate)borate (LiDFOB) as additive to improve the thermal stability of electrolyte for lithium-ion batteries, J. Power Sources (2011), https://doi.org/10.1016/j.jpowsour.2010.10.050.

[49] J.G. Han, J. Bin Lee, A. Cha, T.K. Lee, W. Cho, S. Chae, S.J. Kang, S.K. Kwak, J. Cho, S.Y. Hong, N.S. Choi, Unsymmetrical fluorinated malonatoborate as an amphoteric additive for high-energy-density lithium- ion batteries, Energy Environ. Sci. (2018), https://doi.org/10.1039/c8ee00372f.

[50] K. Schroder, J. Avarado, T.A. Yersak, J.C. Li, N. Dudney, L.J. Webb, Y.S. Meng, K.J. Stevenson, The effect of fluoroethylene carbonate as an additive on the solid electrolyte interphase on silicon lithium-ion electrodes, Chem. Mater. (2015), https://doi.org/10.1021/acs.chemmater.5b01627.

[51] M.C. Biesinger, B.P. Payne, A.P. Grosvenor, L.W.M. Lau, A.R. Gerson, R.S.C. Smart, Resolving surface chemical states in XPS analysis of first row transition metals, oxides and hydroxides: Cr, Mn, Fe, Co and Ni, Appl. Surf. Sci. (2011), https://doi.org/10.1016/j.apsusc.2010.10.051.

[52] W. Li, A. Dolocan, P. Oh, H. Celio, S. Park, J. Cho, A. Manthiram, Dynamic behaviour of interphases and its implication on high-energy-density cathode materials in lithium-ion batteries, Nat. Commun. (2017), https://doi.org/10.1038/ncomms14589.

[53] T. Sui, B. Song, J. Dluhos, L. Lu, A.M. Korsunsky, Nanoscale chemical mapping of Li-ion battery cathode material by FIB-SEM and TOF-SIMS multi-modal microscopy, Nano Energy (2015), https://doi.org/10.1016/j.nanoen.2015.08.013.

[54] E.Y. Hu, X.Q. Yu, R.Q. Lin, X.X. Bi, J. Lu, S.M. Bak, K.W. Nam, H.L.L. Xin, C. Jaye, D.A. Fischer, K. Amine, X.Q. Yang, Evolution of redox couples in Li- and Mn-rich cathode materials and mitigation of voltage fade by reducing oxygen release, Nature Energy (2018), https://doi.org/10.1038/s41560-018-0207-z.

[55] F. Wu, W.K. Li, L. Chen, J. Wang, W.R.G.M.L. Bao, Y. Lu, J. Tan, S. Chen, R.J. Chen, Y.F. Su, Simultaneously fabricating homogeneous nanostructured ionic and electronic pathways for layered lithium-rich oxides, J. Power Sources (2018), https://doi.org/10.1016/j.jpowsour.2018.06.074.

[56] J.M. Zheng, S.J. Myeong, W.R. Cho, P.F. Yan, J. Xiao, C.M. Wang, J. Cho, J.G. Zhang, Li- and Mn-rich cathode materials: challenges to commercialization, Advanced Energy Materials (2017), https://doi.org/10.1002/aenm.201601284.

[57] A. Singer, M. Zhang, S. Hy, D. Cela, C. Fang, T.A. Wynn, B. Qiu, Y. Xia, Z. Liu, A. Ulvestad, N. Hua, J. Wingert, H. Liu, M. Sprung, A.V. Zozulya, E. Maxey, R. Harder, Y.S. Meng, O.G. Shpyrko, Nucleation of dislocations and their dynamics in layered oxide cathode materials during battery charging, Nature Energy (2018), https://doi.org/10.1038/s41560-018-0184-2.